

Random nature of epithelial cancer cell monolayers

Daria S. Roshal, Marianne Martin, Kirill Fedorenko, Ivan Golushko, Virginie Molle, Stephen Baghdiguian, Sergei B. Rochal

▶ **To cite this version:**

Daria S. Roshal, Marianne Martin, Kirill Fedorenko, Ivan Golushko, Virginie Molle, et al.. Random nature of epithelial cancer cell monolayers. Journal of the Royal Society Interface, 2022, 19 (190), 10.1098/rsif.2022.0026 . hal-03676003

HAL Id: hal-03676003
https://hal.science/hal-03676003

Submitted on 23 May 2022

HAL is a multi-disciplinary open access archive for the deposit and dissemination of scientific research documents, whether they are published or not. The documents may come from teaching and research institutions in France or abroad, or from public or private research centers.

L'archive ouverte pluridisciplinaire **HAL**, est destinée au dépôt et à la diffusion de documents scientifiques de niveau recherche, publiés ou non, émanant des établissements d'enseignement et de recherche français ou étrangers, des laboratoires publics ou privés.

Random nature of epithelial cancer cell monolayers

Daria S. Roshal[1*], Marianne Martin[2*], Kirill Fedorenko[1], Ivan Golushko[4], Virginie Molle[2], Stephen Baghdiguian[3] & Sergei B. Rochal[1**]**

*Equal contribution
**Co-last and co-corresponding authors
[1] Faculty of Physics, Southern Federal University, Zorge 5, Rostov-on-Don, 344090, Russian Federation
[2] Laboratory of Pathogen Host Interactions, Université de Montpellier, Centre National de la Recherche Scientifique, UMR 5235, Montpellier, 34095 France
[3] Institut des Sciences de l'Evolution-Montpellier, Université Montpellier, Centre National de la Recherche Scientifique, Ecole Pratique des Hautes Etudes, Institut de Recherche pour le Développement, Montpellier, 34095 France
[4] Research and Education Center "Materials", Don State Technical University, 1 Gagarin Square, Rostov-on-Don, 344000, Russia

Abstract

Although the polygonal shape of epithelial cells has drawn the attention of scientists for several centuries, only a decade and a half ago, it has been demonstrated that distributions of polygon types (DOPTs) are similar in proliferative epithelia of many different plant and animal species. In this study we show that hyper-proliferation of cancer cells disrupts this universal paradigm and results in randomly organized epithelial structures. Examining non-synchronized and synchronized HeLa cervix cells, we suppose that the spread of cell sizes is the main parameter controlling the DOPT in the cancer cell monolayers. To test this hypothesis, we develop a theory of morphologically similar random polygonal packings. By analyzing differences between tumoral and normal epithelial cell monolayers, we conclude that the latter have more ordered structures because of the lower proliferation rates and, consequently, more effective relaxation of mechanical stress associated with cell division and growth. To explain the structural features of normal proliferative epithelium, we take into account the spread of cell sizes in the monolayer. The proposed theory also rationalizes some specific highly ordered post-mitotic unconventional epithelia.

1. Introduction

Symmetry and topology determine the structure and laws of motion for relatively simple abiotic systems studied by physics and chemistry. In living systems, gene expression is usually considered as the fundamental mechanism controlling development and homeostasis [1,2]. Nevertheless, the polygonal (prismatic in 3D) shape of cells, and their highly ordered packing in epithelia, clearly demonstrate that the organization of these cell monolayers directly follows basic physical and topological rules [3-5]. Epithelial growth is achieved by intercalary cell divisions within a constrained volume [6]. Dividing cells change their mediolateral neighbors, thus maintaining the apico-basal architecture and tightness of the intact layer [7], which retains both robustness and plasticity. The most striking phenomenon is the so-called topological invariance observed in almost all proliferative epithelia within phylogenetically distant organisms harboring different global architectures. In fact, during their formation, different epithelial structures converge to polygonal packings with very similar DOPTs [8-12]. Therefore, in very different epithelia the

probabilities to observe cells with the same number of sides are approximately equal. This topological invariance seems to be closely associated with the physiological invariance of epithelium: in all eumetazoans, epithelial structures form a selective paracellular barrier, which controls fluxes of nutrients, regulates ion and water movements, and limits host contact with antigens and microbes. This universal function of epithelia is achieved by the maintenance of the epithelial tightness throughout various morphogenetic processes, like embryonic development, organogenesis, or continuous cell renewal [13-15].

Topology of the cellular borders was first studied back in 1928 [8]. In this pioneer work, the DOPT in the proliferative epithelium of cucumber was investigated: out of 1000 epithelial cells studied, 474 were hexagonal, 251 were pentagonal, and 224 were heptagonal. Later, in an excellent article [11], the hypothesis of topological invariance was formulated. It was established that the similar distributions of polygons are observed in epithelia of several more animal species, and a Markov-type theory was proposed to explain such invariance. This theory assumed that the junction that appears during cell division is always located in such a manner that it forms two additional polygonal vertices, which are necessarily on non-adjacent sides of the original polygon. It was also supposed that the probability of the junction formation is independent of the ratio between the parts in which the cell is divided. Nevertheless, the theory [11-12] cannot explain the existence of 4-valent cells, for which the observed fraction varies from 2 to 3% [8,11]. In addition, this approach considers neither the possibility of cellular motility nor mechanical interactions between cells, which are crucial for the the epithelium properties [16-18].

These facts together with new findings regarding the effect of mechanical stress on the reorganization of focal adhesion, adherent junctions, and cytoskeleton, as well as cell division and growth [10,16,19-21] motivated development of the microscopic models of epithelia. In the last 15 years, several approaches, which consider cells as polygons and define energy of the system as a function of their areas and lengths of their edges, were proposed to explain the influence of mechanics on the topology and collective behavior in cellular monolayers [4, 22-27]. One of the major successes of these models is a discovery of the solid-liquid transition controlled by the effective parameter, so-called target shape index [4,23,24] that is defined by the competition between active contractility of actin–myosin subcellular cortex, cortical tension, and cell-cell adhesion [24]. It has been demonstrated that decrease of the adhesion between cells leads to the "jamming" of the soft liquid-like phase which is accompanied by the increase of the share of six-valent cells and overall ordering of the structure. Experimental observations confirm that epithelial tissues indeed exhibit glassy behavior essential for such processes as embryonic development, cancer metastasis, and wound healing [24]. Normal development of epithelium involves mesenchymal-to-epithelial transition (MET) leading to the dramatic decrease of cell mobility and mitotic rate. At this transition, cells take more regular shapes with smaller average perimeter. The reverse process, leading to the appearance of elongated cells with high mobility, is called the epithelial-to-mesenchymal transition (EMT) [28]; cells undergoing oncogenic EMT are believed to drive metastasis process [29]. In this context, new data on relatively easily measurable geometric parameters of cell monolayers as DOPTs and distribution of cell areas can be helpful to distinguish pathological states and develop theoretical models of cancer and normal epithelia.

In this paper, we investigate the structural characteristics of non-synchronized (conventional) and synchronized confluent monolayers obtained from HeLa epithelial cancer cells. The latter monolayers are of particular interest, since most of the cells constituting this epithelial model belong to the second generation, and the Markov-type theory used in ref. [11] goes beyond the scope of its applicability. Moreover, despite numerous previously published data [30], a putative influence of the cell cycle duration and cell synchronization on the epithelial structure remains unclear [13].

In order to rationalize the observed epithelial structures, we propose a new geometrical model generating polygonal packings that are very similar to the structures observed in non-synchronized and synchronized HeLa monolayers. Testing and applying our approach to several normal proliferative epithelia, we propose the physical mechanism underlying the topological difference

between normal and hyperproliferative epithelia. As we demonstrate, in the epithelia with lower proliferation rates the relaxation of mechanical stresses associated with cell division and cell growth results in more ordered structures and maintains the topological invariance.

2. Results

2.1. Structural characterization of cancer cell monolayers.

Before carrying out the structural characterization of the epithelial monolayers that we obtained, it is important to discuss some general properties of DOPT. Note that the cell polygons in the epithelium are generally convex and form a tessellation of the monolayer surface that is similar to the Voronoi one [31], which, in turn, is a dual of Delaunay triangulation [32]. In this case, for an infinite arbitrary flat monolayer, the average number of nearest neighbors equals 6. Indeed, if the Gaussian curvature is absent, then the equality $\Delta=0$ takes place, where

$$\Delta = \sum_i P_i \cdot (i-6), \qquad (1)$$

$P_i = N_i/\Sigma_j N_j$ is the concentration of cells with i nearest neighbors and N_j is the total number of cells with j nearest neighbors. Recall that the quantity $Q = \sum_i N_i \cdot (i-6)$, proportional to Δ, is called the topological charge [33-35]. For a triangulation of the sphere, Q=12, for a torus, as well as for an infinite plane, Q=0.

In fact, the non-local equality $\Delta=0$ or the equivalent statement about the average number of neighbors means that the DOPT must be balanced: the number of cellular n-gons, with $n<6$, must balance the number of n-gons with $n>6$. In this equilibrium, the weights of 5- and 7-gons are equal to one, the weights of 4- and 8-gons are twice as large, etc. equation (1) can be used to estimate the error in the experimental determination of DOPT. For a finite monolayer, or when averaging over several samples, the obtained value of Δ can deviate from zero, characterizing the error of the experimental method for calculating the DOPT. In particular, due to the relatively large number of cells considered in *Cucumis* epithelium [8], the error (1) for this case is ~0.004, which is almost 10 times lower than for the data in ref. [11]. Nevertheless, in the geometrically correct model of cell division [11], with an increase in the number of successive divisions, Δ tends to 0, reaching $\Delta\approx0.001$ at 10^{th} division. Since both the left and right sides of the distribution contribute to Δ, it is reasonable to estimate the maximum error in determining the probabilities P_i in the DOPT as $\Delta/2$. Also, the condition $\Delta=0$ severely restricts the possible shapes of the DOPT. In real epithelia, probabilities P_i, where $i>7$ or $i<5$, are small. The critical probability is P_6, and other probabilities follow it conserving the condition $\Delta=0$. For example, if in a hypothetical planar epithelium consisting only of 5-,6- and 7-valent cells, the percentage of hexagonal cells is P_6 then concentrations of 5- and 7-valent cells should be equal to $(1-P_6)/2$.

HeLa cells are human malignant epithelial cells derived from an epidermoid carcinoma of the cervix. The growth of confluent HeLa cell monolayers and synchronization procedure are described in Methods, see also electronic supplementary material. In synchronized monolayers, most of the cells belong to the second generation with similar time elapsed after the division process. The characterization of the HeLa and HeLa synchronized epithelia (see figure 1) was carried out using 9 and 7 assembled images obtained by the juxtaposition of contiguous microscope fields. The studied epithelial areas contained from 404 to 933 cells. The first line of figure 1 shows typical non-synchronized and synchronized HeLa epithelial cells (respectively samples HeLa9 and $HeLa_{syn}5$ in Table I). Due to visualization specificities (see Methods), the cell nuclei in micrographs are clearly visible, while the cell boundaries are indistinguishable in most cases. Therefore, in order to determine the number of nearest neighbors and obtain additional structural data, we used the Voronoi tessellation (see Methods) with the nodes located at the centers of the nuclei as shown in the second line of figure 1. That is, strictly speaking, we analyzed not the valency of cells, but the valency of their nuclei. The areas of the epithelial cells were also calculated as the areas of the cells of the Voronoi tessellations.

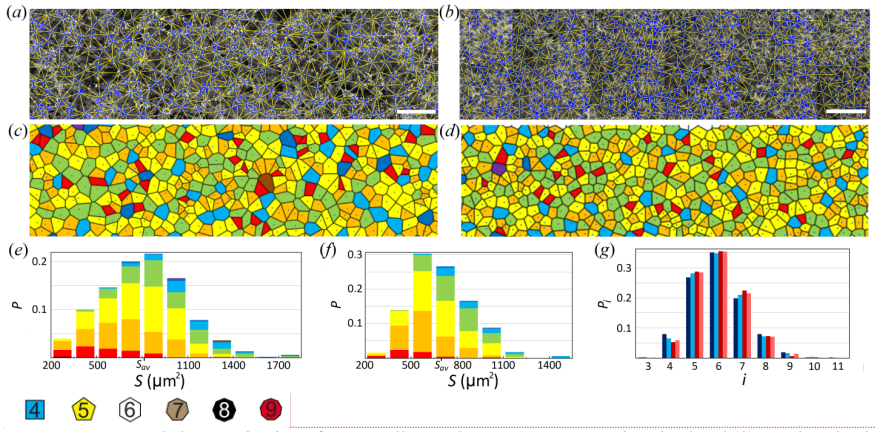


Figure 1. Structural characterization of HeLa cell monolayers. (*a*) Non-synchronized and (*b*) synchronized cellular structures. White scale bars are 100 μm. The triangulation with nodes in the centers of cell nuclei is imposed on the monolayers. (*c*,*d*) Voronoi tessellations for the monolayers (*a*) and (*b*), respectively. Histograms (*e*,*f*) show a probability *P* to observe the certain ranges of cell areas *S* in the samples (*a*,*b*). Polygon types and corresponding contributions to the histograms are color-coded as shown in the legend. (*g*) DOPTs for the samples (*a*,*b*) and averaged data. Dark blue, blue, red, and pink colors correspond to HeLa9, <HeLa>, $HeLa_{syn}5$, and $<HeLa_{syn}>$ lines from Table I. In all cases, the averaged topological error Δ is less than 0.01.

Commenté [РСБ1]: Поднять масштаб (a-d) процентов на 30-40, в 3-ю строчку в два столбика добавить исправленную по цветам легенду в 2 столбца. Убрать не наблюдаемые типы из легенды

To study correlation between DOPTs and the spread of cell sizes we analyzed histograms of cell area distribution for the considered samples (see figure 1(e,f)). All the histograms (including the samples not shown in figure 1) are wide and similar to the Gauss type, which can be explained by the spread of the cell sizes before the mitosis, and the possibility of cell division into substantially unequal parts. Asymmetry of distributions, in our opinion, is due to the fact that in the considered cellular structures, the minimum cell area is limited, not by zero, but by a specific positive value. We have also noticed that the maximum spread of areas strongly fluctuates and can noticeably differ in structures with similar morphology. Therefore, it is reasonable to characterize a cellular structure with the average area S_{av} of its cells and the average spread ΔS, which we define as the difference between the smallest and the largest cell areas among the half of the cells with the areas closest to the S_{av} value. We then introduce a dimensionless effective spread $\Delta S/S_{av}$.

Structural data on the investigated epithelia are presented in Table I. The data in the last two lines are averaged for all the, respectively, synchronized (**<$Hela_{syn}$>**) and non-synchronized (**<HeLa>**) HeLa samples studied. Note, that in 2-4th columns, the values are weighted arithmetic means. Namely, the S_{av}, $\Delta S/S_{av}$ and P_6 values are weighted by the numbers of N_{vor} in each line.

The average cell area in the HeLa non-synchronized epithelium is larger than in the synchronized one (see Table I), since most of the cells in the latter belong to the second generation with similar time elapsed after the division process. In all the examined specimens of both types, the $\Delta S/S_{av}$ value was substantial. The spread in the S_{av} value is apparently due to the growth of samples upon coverslips with an uneven surface. Therefore, the cellular monolayer undergoes a strain, which we consider to be homogeneous in the image size scale. The spread in the average cell areas between the samples of the same type can be also related to the following experimental feature. To prevent the formation of multilayers, the growth is stopped just before the total confluence of the cells. As a result, small and relatively sparse empty areas appear (see Methods). Note also that the averaged value $< \Delta S/S_{av} >$ is 7% larger in the HeLa non-synchronized data set. However, the averaged DOPTs remain very close, with the differences in probabilities $\Delta P_i \lesssim 0.01$ (see figure 1g).

Table I. Characterization of the studied samples. The columns contain: sample name, average area of Voronoi cells $S_{av,}$ dimensionless effective spread of areas $\Delta S/S_{av}$, probability P_6, number of identified Voronoi cells N_{vor}, total number of cells N_{tot}. The last two lines in bold correspond to the averaged structural data (including standard deviations) for HeLa and HeLa synchronized samples.

Code	S_{av} (μm^2)	$\boldsymbol{\Delta S/S_{av}}$	P_6	N_{vor}	N_{tot}
HeLa1	839.0	0.444	0.318	402	578
HeLa2	1024.3	0.388	0.373	263	404
HeLa3bis	951.2	0.431	0.349	373	561
HeLa4	942.8	0.501	0.336	318	532
HeLa5	831.0	0.462	0.348	399	623
HeLa6bis	1057.9	0.388	0.343	539	742
HeLa8	987.9	0.411	0.371	582	780
HeLa9	813.1	0.441	0.352	691	915
HeLa10	923.9	0.444	0.343	577	828
HeLa$_{syn}$1	499.8	0.452	0.379	688	933
HeLa$_{syn}$3	628.9	0.418	0.337	591	826
HeLa$_{syn}$4	853.9	0.391	0.325	409	593
HeLa$_{syn}$5	696.5	0.386	0.355	512	714
HeLa$_{syn}$6	970.3	0.367	0.371	353	525
HeLa$_{syn}$8	815.9	0.378	0.316	396	624
HeLa$_{syn}$9	693.9	0.391	0.372	521	739
<HeLa>	**924.9±100.0**	**0.433±100.0**	**0.348±100.0**	**460.4**	**662.6**
<Hela$_{syn}$>	**705.6±100.0**	**0.403±100.0**	**0.353±100.0**	**495.7**	**707.7**

Commenté [РСБ2]: Посчитай и впиши в таблицу.

2.2. Model of random polygon packing.

As we have already mentioned, synchronized cell monolayers are beyond the scope of applicability of the Markov-type theory [11]. Its inapplicability for the non-synchronized case is evidenced by our finding that DOPTs in both types of monolayers are very similar. Differences in structural parameters of different samples, substantial spread of the cell sizes, and the specific asymmetry of the cell area distributions lead to the hypothesis that in the hyperproliferative epithelia the cell packings are close to random but, nevertheless, satisfy the geometric constraint associated with the existence of minimal cell size. Below we develop the theory of random polygonal packings and then test our hypothesis on epithelial cancer cell monolayers.

To construct the random polygonal packings, we start from random distributions of points with minimal allowed distance between them, d_{min}. We use periodic boundary conditions (which ensure $\Delta=0$) and follow the random sequential adsorption algorithm [36]. Points are randomly and sequentially inserted into the fundamental region with the area A_r. If the distance between the point that is currently being placed and any of the points placed earlier is less than the distance $d_{\min}$, then this point is deleted, and the random insertion is repeated. When the desired N number is achieved, the insertion is stopped. The subsequent Voronoi tessellation yields polygons with the average area $S_{av} = A_r/N$.

Obviously, there exists an averaged maximum limit on the number of points N_{max} that can be randomly placed in the region with area A_r for the given minimal distance d_{min}. Thanks to the discovery of new types of disordered structures and the continuous increase of available computing power, this limit, also known as the jamming limit [36], has been extensively studied in the literature over the past 30 years for various shapes and dimensions of adsorbed particles [36-39]. In the case of the random sequential adsorption of equivalent disks, the average ratio of the area occupied by them to the total surface area tends to $L \approx 0.547$ [36]. Naturally, in our model the average ratio $\pi N_{max} d_{min}^2/A_r$ tends to the same value.

If a packing is not random, its surface coverage can differ significantly. For example, for the densest hexagonal packing of equivalent disks the surface coverage equals $\frac{\pi}{2\sqrt{3}} \approx 0.9064$. Let us consider the densest hexagonal packing with N disks per area A_r. In this packing $d_{min}=d_{hex}$, where $d_{hex}=\sqrt{\frac{4A_r}{N\sqrt{3}}}$ is the distance between the disk centers. Then, in our packing algorithm the jamming limit corresponds to $d_{min}=\sqrt{\frac{2L\sqrt{3}}{\pi}}d_{hex} \approx 0.776 d_{hex}$.

Note that to model the hyperproliferative epithelia we use the unsaturated structures, where the ratio $\eta = d_{min}/d_{hex}$ is smaller than the above critical value 0.776. Figure 2a-f shows examples and area distribution histograms of random polygonal packings with different ratios η and different degrees of hexagonality. The plots in figure 2g are calculated up to η=0.75, since at larger η the calculation time increases sharply. Note also, that packings with the same η can have slightly different morphology, so the averaging is needed. In particular, when N~5000, in the region where η>0.4, the ratio $\Delta S/S_{av}$ and probabilities P_i are reproduced with standard deviations smaller than 0.01 (see figure 2g).

The proposed random packing model is in perfect agreement with the averaged structural data for the non-synchronized and synchronized HeLa epithelial cell monolayers (see the last two lines of Table I (**<Hela>** and **<Hela$_{syn}$>**) and the histograms in figure 1g). Indeed, as presented in figure 2g, the change in $\Delta S/S_{av}$ from 0.4 to 0.43 corresponds to the variation of η from 0.5 to 0.47, respectively. In this region, the slope of the plot $P_6(\eta)$ is small, and the values of η correspond to very close DOPTs with $P_6 \approx 0.35 - 0.37$. The deviations of other averaged probabilities (see figure 1g) from their theoretical values also do not exceed 0.02, which is within the spread of model calculations at N~5000.

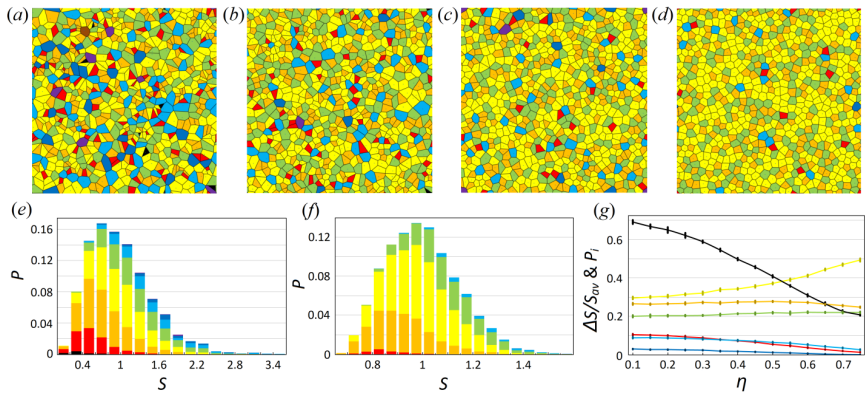


Figure 2. Examples of random packings and their geometric characteristics. (*a-d*) Packings obtained at η values equal to 0.1, 0.4, 0.6, and 0.758, respectively. It can be observed how the fraction of hexagonal cells grows with increasing η (these cells are shown in yellow; the coloring is the same as in figures 1c-f). (*e-f*) Area distribution histograms obtained for η=0.1 and 0.758. For both cases, the value of S_{av} is renormalized to 1. (*g*) Dependences $\Delta S/S_{av}$ and P_i on η. Plots of $\Delta S/S_{av}$, P_6, P_5, P_7, P_4, P_8, P_9, calculated with the step $\Delta\eta$=0.05, are colored with black, yellow, orange, green, red, light blue and dark blue colors, respectively. Probabilities P_3, P_{10} and P_{11} are too small to be shown in the chosen scale. Each center of vertical bars represents the averaging of 10 calculations at N=5000. The bar sizes denote the standard deviations obtained for the calculations.

The random packing model can also explain the scatter of $\Delta S/S_{av}$ and P_6 values between different samples presented in Table I. Note that these monolayers contain, on average, slightly less than 500 cells, and such a small value of N increases the morphological inhomogeneity of the

generated packings. To justify this, one can perform a series of computations with the appropriate inputs: the number of calculations should not be less than the total number of monolayers, and N is equal to N_{vor} in the sample. As a result, it is highly probable that a packing that deviates from the mean by about (or even more) than the considered sample will be generated.

As we already mentioned, small and relatively sparse empty domains are present in non-synchronized HeLa monolayers. We decided to evaluate the impact of these domains on the obtained results. For this purpose, on the assembled images, we selected 40 smaller regions without empty areas. These confluent rectangular regions contained from 36 to 76 cells. When averaging over these regions, the values of S_{av} were found separately, and cells for which it was impossible to determine the number of nearest neighbors were not considered. This treatment resulted in $\Delta S/S_{av} \approx 0.394$ and $P_6 \approx 0.38$. Comparing these values with those for averaged **<HeLa>** and using the graphs shown in figure 2g, we observe that the decrease in $\Delta S/S_{av}$ corresponds to the small increase in P_6, and the order is still properly described by the developed theory of random polygonal packings. So, we conclude that both types of considered hyperproliferative epithelia represent the random packings, while the main structural difference between the non-synchronized and synchronized HeLa monolayers consists in different values of S_{av}.

3. Discussion

In the literature, one can find many biophysical approaches describing the correlation between epithelial properties and averaged cell area and perimeter (see, for example, [4,16,23,24,26,27,40]). The spread in these geometrical parameters is often considered as a 'biological noise' and its importance for the epithelium is discussed in only handful of papers [34,40-42]. In particular, the recent paper [41] demonstrates that the relation between average aspect ratio of the cells comprising epithelium and its standard deviation governs processes as diverse as maturation of the pseudostratified bronchial epithelial layer cultured from non-asthmatic or asthmatic donors, and formation of the ventral furrow in the Drosophila embryo. Interestingly, in the paper [40] a possibility of a similar connection between cell area variability and DOPT was only briefly mentioned. In our paper, as far as we know, we have for the first time proposed a model that establishes the relation between the cell size spread $\Delta S/S_{av}$ and DOPT in the cancer epithelial monolayers. Examining non-synchronized and synchronized HeLa cervix cells, we have shown that this spread is the main parameter controlling the DOPT in both types of the monolayers that represent a real-life example of random packings.

Below we discuss how a healthy proliferative epithelium distinguishes from random cancer monolayers and point out a physical mechanism underlying this difference. As one can see from figure 2g, at η~0.62−0.7, the model of random polygon packing reproduces perfectly the DOPTs [8-11] typical of many plant and animal proliferative epithelia: $P_4 \approx 0.02 - 0.03$, $P_5 \approx 0.25 - 0.27$, $P_6 \approx 0.41 - 0.47$, $P_7 \approx 0.22$, $P_8 \approx 0.03 - 0.05$, and $P_9 \approx 0.001 - 0.006$. A more detailed analysis, however, shows that the proposed approach leads to a value of $\Delta S/S_{av}$ that is slightly smaller than the one observed experimentally. In particular, after analyzing the images of the *Cucumis* proliferative epithelium [8], we have estimated the value of $\Delta S/S_{av}$ as 0.29, which in the random polygon packing model corresponds to η~0.63 and $P_6 \approx 0.43$ instead of the observed value $P_6 \approx 0.47$ [8].

Let us consider the situation in more detail using our experimental data on healthy proliferative Human Cervical Epithelial Cells (HCerEpiC). Figure 3a-b demonstrates a typical sample of HCerEpiC confluent monolayer with the corresponding Delaunay triangulation and Voronoi tessellation. Forty analogous experimental images, previously obtained in our laboratory, capture relatively small separate fragments showing simultaneously from 30 to 54 cells.

Note that borders of the HCerEpiC cells are more clearly visible than those of HeLa cells, and thus can be determined directly, without using Voronoi tessellation. First, we analyzed the images following the same procedure we used for HeLa cells. In this way we have obtained the following structural data: $S_{av} \approx 3.0 \times 10^3$ μm^2, $\Delta S/S_{av} \approx 0.43$, $P_4 \approx 0.04$, $P_5 \approx 0.30$, $P_6 \approx 0.41$, $P_7 \approx 0.20$,

P_8≈0.04, and P_9≈0.01. It is interesting to note that these P_i values differ from those obtained for the *Xenopus* frog [11] by less than 2% and the HCerEpiC epithelium, as expected, has a structure typical of other normal proliferative epithelia [8-11]. We then analyzed the same forty images directly, without using Voronoi tessellation. Although cells with common borders are not necessary linked in the Delaunay triangulation (discrepancy ≈15% of cases), the resulting difference in the calculated average structural parameters is several times smaller indicating compatibility of these two methods. Therefore, below we refer only to the structural data obtained using Voronoi tessellation.

We have also considered the fact that the S_{av} value can vary from one HCerEpiC monolayer fragment to another, because of the influence of the substrate it was grown on. With the averaging method taking this difference into account, the ratio $\Delta S/S_{av}$ decreases from 0.43 down to 0.36, corresponding in the random packing model to P_6≈0.37 (instead of 0.37). Nevertheless, this slightly increased probability is still smaller than the observed value P_6 ≈0.41. Consequently, based on the *Cucumis* and HCerEpiC examples, we can conclude that in normal proliferative epithelia the P_6 value is greater than the one predicted by the random packing model for the same $\Delta S/S_{av}$ ratio.

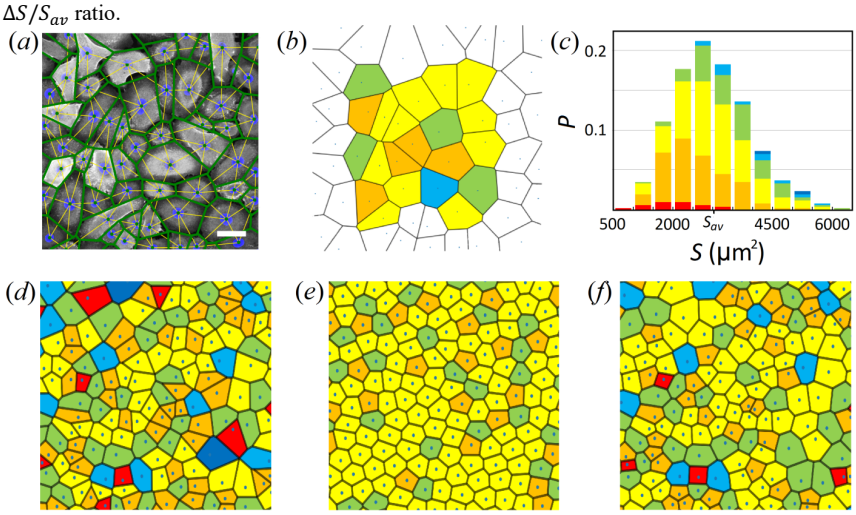


Figure 3. Structural characterization of HCerEpiC epithelium. (*a*) Typical sample of the epithelium with the superimposed triangulation; white scale bar is 50 μm. Vertices of the Delaunay triangulation coincide with the cell nuclei. The borders between the cells are shown in green. (*b*) Dual Voronoi tessellation for the same sample. A cell was taken into account in the statistical analysis if its shape could be determined unambiguously and the cell vertices were not too close to the border of the image (see Methods). Such cells are colored. (*c*) Averaged histogram of cell areas in forty samples. (*d*) Voronoi tiling for a random polygonal structure with the same $\Delta S/S_{av}$ value and very similar to (*c*) histogram of the cell area distribution. The polygon coloring is the same as in figures 1c-f (*e,f*). More ordered structures obtained from (*d*) by minimizing the model energies of elastic intercellular interaction (see main text). (*e*) Minimization of energy (3) at $\beta S_{av}/\zeta$=1 and q=3.81 results in a highly ordered structure with $P_6 \approx 0.7$. (*f*) Minimization of energy (4) at $\beta S_{av}/\zeta$=10 and q=3.81 yields the packing structurally similar to HCerEpiC epithelium: $\Delta S/S_{av} \approx 0.45$ and $P_6 \approx 0.41$.

Note that the mitosis rate in HeLa cells is ~5.5 times higher than in HCerEpiC cells, while the rate of apoptosis is the same in both cases (see electronic supplementary material, figure S1). Due to this difference, for the same number of seeded cells, the considered monolayers are at confluence after 2 days for HeLa cells compared to 4 days for HCerEpiC ones. Thus, we can

assume that the P_6 increase in healthy epithelium is associated with the lower rate of cell division, although, intercellular interactions are also very important for this phenomenon.

To justify the latter statement, we recall that ordering of equivalent particles, retained on a planar surface and interacting with each other via very different pair potentials, readily leads to the formation of a simple hexagonal order [35]. In our opinion, the mechanism of the P_6 increase in healthy proliferative epithelia is similar and caused by minimization of the elastic energy associated with the mechanical interaction between cells. Namely, an internal local stress caused by the cell division and nonuniform growth can relax through cell motility, which increases, in average, the hexagonal coordination.

Below, we consider a simple way to demonstrate that mechanical interactions between cells can order the epithelial structure by increasing the number of cells with six neighbors. Following the works [23,24], the elastic deformation energy E of a monolayer containing N cells can be written as:

$$E = \sum_{i=1}^{N} \beta_i \left(A_i - A_i^0\right)^2 + \zeta_i \left(P_i - P_i^0\right)^2, \quad (2)$$

where the subscript i labels each cell; A_i and P_i are the cell area and perimeter, respectively. The origin of the elastic moduli β_i is associated with a combination of the cell volume incompressibility and resistance to height differences between nearest cells [24]. The second term including the cell perimeters P_i results from active contractility of the actomyosin subcellular cortex (quadratic in P_i) and effective cell membrane tension due to cell-cell adhesion and cortical tension, which are linear in perimeter. Usually, different cells of the same type are assumed to have the same elastic moduli β_i and ζ_i and thus index 'i' is omitted. The same goes for the parameters P_i^0 and A_i^0, which are usually substituted with P_{eff} and S_{av}, correspondingly. The resulting energy reads:

$$E = \sum_{i=1}^{N} \beta \left(A_i - S_{av}\right)^2 + \zeta \left(P_i - P_{eff}\right)^2. \quad (3)$$

In [24], using the Surface Evolver software [43], the energy (3) was minimized with respect to the position and shape of the intercellular boundaries, while in [23] an overdamped dynamic model was built. The latter model takes into account the effective temperature of the monolayer, which corresponds to the value of additional (not related to intercellular interaction (3)) random forces simulating active cell migration. In the model [23], the shape of the cells coincides with the shape of Voronoi cells therefore the energy (3) depends only on positions of the Voronoi cells centers. The results of the works [23,24] are similar, and the properties of both models depend on so-called target shape index $q = \frac{P_{eff}}{\sqrt{S_{av}}}$ [23,24]. To clarify the meaning of this quantity, note that for the regular honeycomb packing the quantity $q = \frac{6}{\sqrt{1.5\sqrt{3}}} \approx 3.72$, while $q = 4$ and $q \approx 4.56$ minimize the energy (3) for regular square and triangular lattices, respectively. As shown in the works [23,24] at $q>q_0$, where q_0=3.81−3.813, the cells acquire the possibility of relative movement without overcoming the potential barrier, and the monolayer demonstrates the fluid-like behavior [23,24]. At the same time, as can be seen from the model monolayers presented in these works, at $q>q_0$ the number of 6-valent cells decreases, and many cells acquire an elongated shape.

Since our analysis of experimental data is also based on the Voronoi tiling, let us discuss the results [23] in more detail. Image analysis (see figure 2b in [23]) reveals that $\Delta S/S_{av}$ are 0.1 and 0.12, respectively, for the solid and liquid states of the model monolayers shown. However, even in *Cucumis* epithelium, the most ordered proliferative monolayer considered in our work, $\Delta S/S_{av}$ ≈0.29, which is almost 3 times more than in the model structures [23]. Also note that the probability of P_6 in the solid phase [23] (its comparing with normal epithelium is reasonable) is 0.595, whereas for ordinary proliferative epithelia, the value of P_6 lies in the range of 0.41-0.47 [8-11].

To assess the influence of cell-to-cell interactions on the DOPT in the model [23], we performed a series of numerical experiments, where the energy (3) was minimized using the ordinary

coordinate descent method. As the initial positions of N=400 cell centers, we used random coordinates obtained within the framework of the above algorithm for constructing random polygonal packings. The analysis showed that mechanical intercellular interactions can strongly order the system. In the region $q<q_0$, depending on the initial positions of the particles and the ratio of the coefficients $0.01< \beta S_{av}/\zeta<100$, minimization of (3) led to the probabilities $P_6 = 0.6 - 0.8$ (see figure 3e). The scatter of the obtained P_6 values is associated not only with the change in the model parameters, but also with the existence of numerous local energy minima. Note that the anomalous epithelia with $P_6 \approx 0.6-0.9$ are also observed in nature. For example, after the mitosis in the wings of a *Drosophila* stops (and before the start of hair growth), the equilibrium changes and a sharp increase in the proportion of 6-valent cells occurs [40]. As our preliminary estimates show, the use of Lennard-Jones potential [44] to describe the intercellular interaction and assumption of the cell size dispersion [34] allow to obtain epithelium-like structures with P_6 up to the level of 0.9.

Rationalization of normal proliferative epithelia within the framework [23] is problematic not only due to the significant effective temperature and monolayer disordering required to reduce the probability P_6 from $0.6-0.8$ to $0.4-0.47$. The assumption of the same equilibrium area S_{av} for all cells (made in equation (3)) limits the ability of the model to generate structures with realistic values of $\Delta S/S_{av}$. In this context, transition from energy (2) to (3) by replacing A_i^0, P_i^0 with corresponding averages seems to be an oversimplification; thus, we use the following energy instead:

$$E = \sum_{i=1}^{N} \beta (A_i - A_i^0)^2 + \zeta \left(P_i - q \sqrt{\overline{A_i^0}} \right)^2, \qquad (4)$$

where the equilibrium areas A_i^0 are defined by our random polygonal packing model.

Methods to analyze an energy landscape are known [42,45], nevertheless, for energy (4) it is a separate complex problem, since the energy (4) has a huge number of local minima with different DOPTs. We have only verified that minimization of this energy approximately preserves the initial value of $\Delta S/S_{av}$, and in the region $q < q_0$, leads to an increase in P_6 that is smaller than the one occurring during the minimization of energy (3).

Using the energy (4), one can more realistically simulate normal proliferative epithelia, in particular HCerEpiC epithelium. The DOPT in HCerEpiC epithelium corresponds to the random polygonal packing with $\eta \approx 0.62$, while the observed $\Delta S/S_{av}$ corresponds to $\eta \approx 0.53$. To correct the DOPT, we generated a random polygonal structure with $\eta \approx 0.53$ (see figure 3d), that yields a distribution of cell areas very close to that of the HCerEpiC epithelium (see figure 3c). At q=3.81, we minimized energy (4) at different ratios $\beta S_{av}/\zeta$ in the region $0.01 - 100$. This gave rise to structures with $P_6 = 0.38 - 0.43$. One of these structures, closest to the HCerEpiC epithelium, is shown in figure 3f.

Finally, we note that in epithelia there are multiple processes brining system out of equilibrium such as mitosis, apoptosis, varying cell growth rate. Their influence on DOPT cannot be taken in account by the simple minimization of energy (4). The construction of such a more complex dynamic model is clearly beyond the scope of this work and is a task for the next studies.

4. Conclusion

In this paper, we have demonstrated the significant difference in topology of cancerous and normal epithelial monolayers. In epithelial cancer monolayers, the cell arrangement is close to random but, nevertheless, satisfies the geometric constraint associated with the existence of minimal cell size. This type of the cell order can be described with a good accuracy by a single dimensionless control parameter, namely the normalized halfwidth $\Delta S/S_{av}$ of the cell area distribution. Cancer

cells divide so quickly that the relaxation processes associated with the minimization of free energy are unable to effectively rearrange cells and order the monolayer by increasing the number of 6-valent cells. Consequently, the growing disorder predominates over the intercellular interactions, and this yields structures very similar to random polygonal packings. In contrast, normal proliferative and non-proliferative epithelia are morphologically different from them. Overall, our study of epithelial monolayers provides novel mathematical tools for a topological analysis of epithelial morphogenesis in a developmental and/or pathological context. In particular, elaborated tools could be used to analyze the change in cell topology during the 2D/3D transition observed throughout epithelial tumorigenesis. In the near future, we hope to apply our approach to studing the zebrafish embryonic epidermis development before and after tumor cell injection in vivo.

5. Methods

5.1. Cell line growth and synchronization procedure conditions.

Human cervical cancer cell line HeLa was purchased from the American Type Culture Collection (ATCC; Manassas, VA, USA) and maintained in DMEM, high glucose (Dulbecco's Modified Eagle Medium) containing 5% heat-inactivated foetal bovine serum and supplemented with GlutaMAX^{TM} (Gibco Life Technologies), penicillin (100 units/mL), and streptomycin (100 µg/mL). Normal primary cervical epithelial cells (HCerEpiC) isolated from human uterus were purchased from ScienCell Research Laboratories (Clinisciences S.A.S., Nanterre, France). HCerEpic cells were grown in Cervical Epithelial Cell Medium according to the manufacturer's instructions. Cells were incubated in a humidified incubator at 37°C in 5% CO_2.

For confocal microscopy analysis of non-synchronized cells, HeLa or HCerEpiC cells were seeded on glass coverslips (12mm diameter round) coated with 10µg/ml of poly-L-Lysine (P4707, Sigma) at $7{\cdot}10^4$ cells/coverslip in a 24-well culture plate. Confluency of the monolayer was achieved 48 h and 4 days later for HeLa and HCerEpiC cells, respectively. HeLa cells were synchronized in G0/G1 phase of the cell cycle using the double thymidine block procedure. The day before the first thymidine block, cells were seeded on poly-L-Lysine treated glass coverslip at a density of $7.5x10^4$ cells/ coverslip. The next day, 2.5 mM thymidine was added for 16 h (first block). Then cells were washed with phosphate-buffered saline (PBS) and incubated during 8 h without thymidine. Lastly, the second thymidine block was applied for 16h. At the end of the second thymidine block, cells were washed and incubated for 2 additional hours, after which cells were treated with antibodies and analysed by confocal microscopy. Following this procedure, cells are fully confluent and cell synchronisation in G0/G1 is about 92%. This was confirmed by cytofluorometry analysis (FACS) (see electronic supplementary material, figure S2).

5.2. Immunocytochemistry and fluorescence microscopy.

Cells cultured on glass coverslips were fixed with 4% paraformaldehyde in PBS for 20 min, and washed in Tris-buffered saline (25mM Tris pH7.4, 150mM NaCl) (TS) for 10 min. After permeabilization with 0.2% Triton X-100 in TS for 4 min, non-specific binding was blocked with 0.2% gelatin from cold water fish skin (#G7765 Sigma-Aldrich Chimie, Lyon) in TS for 30min. Cells were incubated with primary antibodies in blocking buffer for 1h and then washed 3 times with 0.008% TritonX-100 in TS for 10 minutes. Rabbit anti-ezrin antibody [46] was used to visualize cell body and membrane. Cells were incubated for 30 minutes with Alexa-Fluor 488 - labelled secondary antibodies (P36934-Molecular Probes, InVitrogen) in blocking buffer. After rinsing in washing buffer, cell nuclei were stained with 1 µg/ml Hoechst 33342 (62249-Thermo Scientific Pierce) in TS for 5 minutes. Finally, coverslips were mounted with Prolong^{TM} Gold Antifade (P36934-Molecular Probes, InVitrogen) and examined under a Leica TCS SPE confocal microscope equipped with a 25X/0.75 PL FLUOTAR oil objective (HCerEpiC) and a 40X/1.15 ACS APO oil objective (HeLa) (figure 3 and electronic supplementary material, figure S1). In the case of HeLa cells (figure 1a) and synchronized HeLa cells (figure 1b), the analysis was performed with a Zeiss LSM880 FastAiryScan confocal microscope equipped with a 40X/1.4 Oil Plan-apochromat DIC objective.

Between 7 to 9 'z-stacks' (0.457µm thickness each) were acquired per field and a 2D image was generated by applying Maximum Intensity Projection processing. For each coverslip, the acquisition pattern was 6 neighbouring images per row for a total of 2 or 3 rows. The resulting images (12 or 18 images) were adjusted for brightness, contrast and color balance by using ImageJ and assembled side by side in PowerPoint to reconstruct a cell monolayer consisting of N>500 cells.

5.3. Image analysis.

After determining the geometric centers of the cell nuclei, triangulation was performed by the Delaunay method [31]. Next, Voronoi tiling was constructed, and the areas of the epithelial cells were calculated as the areas of Voronoi cells. Obviously, for a correct statistical analysis, it is necessary to discard the cells (located too close to the image border), the number of neighbors for which cannot be determined. Note that even if it is possible to construct a closed Voronoi cell, then it is also necessary to check whether the cell polygon boundary can be changed by additional hypothetical nuclei lying directly outside the image border. Therefore, the center of a reliably constructed Voronoi cell should be located at least twice as far from the image border as any of the vertices of this cell. However, this method leads to the appearance of an excessive total positive topological charge, which is localized at the image border. On one hand, 4- and 5-valent cells have a smaller area [8], while on the other hand, the smaller the cell located near the image border, the more chances its nucleus has to satisfy the selection criterion formulated above. This fact, when processing images with a small number of nuclei (about 40), leads on average to the formation of a 5% preponderance of the total positive topological charge (which is carried by 4- and 5-valent cells) over the total negative topological charge. This, in turn, leads to errors when constructing DOPTs diagrams and determining the value of P_6 and $\Delta S/S_{av}$. To avoid preferential selection of small cells, we used additional cutting of the image borders. In the statistical analysis, we took into account only cells whose nuclei centers fall within the rectangle, which has maximum possible size and does not contain any nucleus with an uncertain coordination. Thus, it is possible to significantly reduce the total topological charge of the images and, accordingly, the error in the values of $\Delta S/S_{av}$.

Author contributions. To explain the topological universality of normal epithelia, S.B. proposed to study the cancer cell monolayers. S.R. developed the model of random polygonal packings and controlled the theoretical part of the project. M. M. performed the biological experiments and the confocal microscopy acquisition as well as assembly of images. K.F. realized the initial analysis of images. D.R. did most of the calculations and analysis. I.G. reproduced the SPV computer model and found the relation between our approach and RSA algorithm. S.R. wrote with the essential help of S.B. I.G. and M.M. the main part of the text. V.M. proofread and corrected the article extensively. All authors participated in discussion and writing of the article.

Competing interests. The authors declare no competing interests.

Acknowledgments. M. M., V.M., and S.B. acknowledge the imaging facility MRI, member of the national infrastructure France-BioImaging infrastructure supported by the French National Research Agency (ANR-10-INBS-04, «Investments for the future»). S.R. and D.R. acknowledge the financial support from the Russian Foundation for Basic Research (Grant № 19–32–90134). I.G. acknowledge Russian Science Foundation for the financial support of the research (Grant № 20-72-00164). We thank A. Parmeggiani for useful discussions.

References

1. García-Bellido A. 1975 Genetic control of wing disc development in Drosophila. *Ciba Found Symp.* **29**, 161–182. (doi:10.1002/9780470720110.ch8)

2. Da Silva JF, Williams, RJP. 2001 The biological chemistry of the elements: the inorganic chemistry of life. *Oxford University Press, NY, 2nd edition*.
3. Azzag K. *et al.* 2015 The non-proliferative nature of ascidian folliculogenesis as a model of highly ordered cellular topology distinct from proliferative epithelia. *PLoS One* **10**, e0126341. (doi:10.1371/journal.pone.0126341)
4. Farhadifar R, Röper JC, Aigouy B, Eaton S, Jülicher F. 2007 The influence of cell mechanics, cell-cell interactions, and proliferation on epithelial packing. *Curr. Biol.* **17**, 2095-2104. (doi:10.1016/j.cub.2007.11.049)
5. Nagpal R, Patel A, Gibson MC. 2008 Epithelial topology. *BioEssays* **30**, 260-266. (doi:10.1002/bies.20722)
6. Rauzi M. 2020 Cell intercalation in a simple epithelium. *Philos Trans R Soc Lond B Biol Sci.* **375**, 20190552. (doi:10.1098/rstb.2019.0552)
7. Gibson WT, Gibson MC. 2009 Cell Topology, Geometry, and Morphogenesis in Proliferating Epithelia. *Curr Top Dev Biol.* **89**, 87-114. (doi:10.1016/S0070-2153(09)89004-2)
8. Lewis FT. 1926 The effect of cell division on the shape and size of hexagonal cells. *Anat. Rec.* **l**, 331-355. (doi:10.1002/ar.1090330502)
9. Korn R, Spalding R. 1973 The geometry of plant epidermal cells. *New Phytologist.* **72**, 1357–1365. (doi:10.1111/j.1469-8137.1973.tb02114.x)
10. Kwiatkowska D, Dumais J. 2003 Growth and morphogenesis at the vegetative shoot apex of Anagallis arvensis. *J Exp Bot.* **54**, 1585–1595. (doi:10.1093/jxb/erg166)
11. Gibson MC, Patel AB, Nagpal R, Perrimon N. 2006 The emergence of geometric order in proliferating metazoan epithelia. *Nature* **442**, 1038-1041. (doi:10.1038/nature05014)
12. Patel AB, Gibson WT, Gibson MC, Nagpal R. 2009 Modeling and inferring cleavage patterns in proliferating epithelia. *PLoS Comput. Biol.* **5**, e1000412. (doi:10.1371/journal.pcbi.1000412)
13. Axelrod JD. 2006 Cell shape in proliferating epithelia: a multifaceted problem. *Cell* **126**, 643-645. (doi:10.1016/j.cell.2006.07.018)
14. Chelakkot C, Ghim J, Ryu SH. 2018 Mechanisms regulating intestinal barrier integrity and its pathological implications. *Exp. Mol. Med.* **50**, 1-9. (doi:10.1038/s12276-018-0126-x)
15. Higashi T, Arnold TR, Stephenson RE, Dinshaw KM, Miller AL. 2016 Maintenance of the epithelial barrier and remodeling of cell-cell junctions during cytokinesis. *Current Biology* **26**, 1829-1842. (doi:10.1016/j.cub.2016.05.036)
16. Puliafito A. *et al.* 2012 Collective and single cell behavior in epithelial contact inhibition. *Proc. Natl Acad. Sci. USA*. **109**, 739–744 (doi:10.1073/pnas.1007809109).
17. Angelini TE. *et al.* 2011 Glass-like dynamics of collective cell migration. *Proc. Natl Acad. Sci. USA*. **108**, 4714–4719. (doi:10.1073/pnas.1010059108)
18. Alt S, Ganguly P, Salbreux G. 2017 Vertex models: from cell mechanics to tissue morphogenesis. *Phil. Trans. R. Soc. B*. **372**, 20150520. (doi:10.1098/rstb.2015.0520)
19. Ingber DE. 2006 Cellular mechanotransduction: putting all the pieces together again. *The FASEB journal*, **20**, 811-827. (doi: 10.1096/fj.05-5424rev)
20. Yeung T, et al. 2005 Effects of substrate stiffness on cell morphology, cytoskeletal structure, and adhesion. *Cell Motil. Cytoskeleton* **60**, 24–34. (doi:10.1002/cm.20041)
21. Janmey PA, McCulloch CA. 2007 Cell mechanics: Integrating cell responses to mechanical stimuli. *Annu. Rev. Biomed. Eng.* **9**, 1–34. (doi:10.1146/annurev.bioeng.9.060906.151927)
22. Fletcher AG, Osterfield M, Baker RE, Shvartsman SY. 2014 Vertex models of epithelial morphogenesis. *Biophys. J.* **106**, 2291-2304. (doi:10.1016/j.bpj.2013.11.4498)

23. Bi D, Yang X, Marchetti, MC, Manning ML. 2016 Motility-driven glass and jamming transitions in biological tissues. *Phys. Rev. X* **6**, 021011. (doi:10.1103/PhysRevX.6.021011)
24. Bi D, Lopez JH, Schwarz JM, Manning ML. 2015 A density-independent rigidity transition in biological tissues. *Nat. Phys.* **11**, 1074–1079. (doi:10.1038/nphys3471)
25. Staple DB, Farhadifar R, Röper JC, Aigouy B, Eaton S, Jülicher F. 2010 Mechanics and remodelling of cell packings in epithelia. *Eur. Phys. J. E* **33**, 117–127. (doi:10.1140/epje/i2010-10677-0)
26. Giavazzi F, et al. 2018 Flocking transitions in confluent tissues. *Soft Matter* **14**, 3471–3477. (doi:10.1039/C8SM00126J)
27. Li Y, Naveed H, Kachalo S, Xu LX, Liang J. 2012 Mechanisms of regulating cell topology in proliferating epithelia: Impact of division plane, mechanical forces, and cell memory. *PLoS One* **7**, e43108. (doi:10.1371/journal.pone.0043108)
28. Chaffer CL, Thompson EW, Williams ED. 2007 Mesenchymal to epithelial transition in development and disease. *Cells. Tissues. Organs* **185**, 7–19. (doi:10.1159/000101298)
29. Thompson EW, Newgreen DF. 2005 Carcinoma Invasion and Metastasis: A Role for Epithelial-Mesenchymal Transition? *Cancer Res.* **65**, 5991–5995. (doi:10.1158/0008-5472.CAN-05-0616)
30. Gómez-Gálvez P, Vicente-Munuera P, Anbari S, Buceta J, Escudero LM. 2021 The complex three-dimensional organization of epithelial tissues. *Development* **148**, dev195669. (doi:10.1242/dev.195669)
31. Delaunay B. 1934 Sur la sphère vide: A la mémoire de Georges Voronoi (French). *Izv. Akad. Nauk SSSR, Otdelenie Matematicheskih i Estestvennyh Nauk* **7**, 793–800.
32. Okabe A, Boots B, Sugihara K. 1992 Spatial tessellations: concepts and applications of voronoi diagrams. Wiley, New York.
33. Conway JH, Sloane NJA. 1999 Sphere packings, lattices and groups. Springer, Vol. 290. (doi:10.1007/978-1-4757-2249-9)
34. Roshal DS, Azzag K, Le Goff E, Rochal SB, Baghdiguian S. 2020 Crystal-like order and defects in metazoan epithelia with spherical geometry. *Sci. Rep.* **10**, 7652. (doi:10.1038/s41598-020-64598-w)
35. Roshal DS, Petrov KYu, Myasnikova AE, Rochal SB. 2014 Extended topological defects as sources and outlets of dislocations in spherical hexagonal crystals. *Phys. Lett. A* **378**, 1548-1552. (doi:10.1016/j.physleta.2014.03.037)
36. Feder J. 1980. Random sequential adsorption. *Journal of Theoretical Biology*, **87**, 237-254. (doi:10.1016/0022-5193(80)90358-6)
37. Penrose MD. 2001 Random Parking, Sequential Adsorption, and the Jamming Limit. *Commun. Math. Phys.*, **218**, 153-176. (doi:10.1007/s002200100387)
38. Evans JW. 1993 Random and cooperative sequential adsorption. *Reviews of modern physics*, **65**, 1281. (doi:10.1103/RevModPhys.65.1281)
39. Talbot J, Tarjus G, Van Tassel PR, Viot P. 2000 From car parking to protein adsorption: an overview of sequential adsorption processes. *Colloids Surf. A Physicochem. Eng. Asp.*, **165**, 287-324. (doi:10.1016/S0927-7757(99)00409-4)
40. Classen AK, Anderson KI, Marois E, Eaton S. 2005 Hexagonal packing of Drosophila wing epithelial cells by the planar cell polarity pathway. *Dev. Cell* **9**, 805–817. (doi:10.1016/j.devcel.2005.10.016)
41. Atia L, *et. al.* 2018 Geometric constraints during epithelial jamming. *Nature physics*, *14*(6), 613-620. (doi:10.1038/s41567-018-0089-9)

42. Ballard AF, Panter JR, Wales DJ. 2021 The energy landscapes of bidisperse particle assemblies on a sphere. Soft Matter, **17**, 9019-9027. (doi:10.1039/D1SM01140E)
43. Brakke KA. 1992 The Surface Evolver. Exp. Math. 1, 141–165. (doi:10.1080/10586458.1992.10504253)
44. Martinand-Mari C., et. al. 2009 Topological control of life and death in non-proliferative epithelia. *PLoS One* **4**, e4202. (doi:10.1371/journal.pone.0004202)
45. Wales D. 2003 Energy landscapes: Applications to clusters, biomolecules and glasses. *Cambridge University Press*.
46. Andréoli C, Martin M, Le Borgne R, Reggio H, Mangeat P. 1994 Ezrin has properties to self-associate at the plasma membrane. *J. Cell Sci.* **107**, 2509-2521. (doi:10.1242/jcs.107.9.2509)